

# Memristive deep belief neural network by silicon synapses

Wei Wang<sup>1,4</sup>, Loai Danial<sup>1,5</sup>, Yang Li<sup>1</sup>, Eric Herbelin<sup>1</sup>, Evgeny Pikhay<sup>2</sup>, Yakov Roizin<sup>2</sup>, Barak Hoffer<sup>1</sup>, Zhongrui Wang<sup>3</sup>, Shahar Kvatinsky<sup>1,\*</sup>

<sup>1</sup> The Andrew and Erna Viterbi Faculty of Electrical and Computer Engineering, Technion-Israel Institute of Technology, Haifa, Israel 3200003

<sup>2</sup> Tower Semiconductor, Migdal HaEmek, Israel 2310502

<sup>3</sup> Department of Electrical and Electronic Engineering, The University of Hong Kong, Pokfulam Road, Hong Kong

<sup>4</sup> Current address: Peng Cheng Laboratory, Shenzhen, China; Email: [wangwei@pcl.ac.cn](mailto:wangwei@pcl.ac.cn)

<sup>5</sup> Current address: Intel Corporation, IDC, Haifa, Israel

\* Email: [shahar@ee.technion.ac.il](mailto:shahar@ee.technion.ac.il)

## ABSTRACT

Memristor-based neuromorphic computing systems address the memory-wall issue in von Neumann architecture that prevents the efficient training of deep neural networks (DNNs). Nevertheless, emerging memristor devices, with the existence of several non-idealities, such as poor yield and limited number of reliable conductance states, are still not mature for practical neuromorphic systems. At the same time, the mainstream neuromorphic DNNs utilize the error backpropagation-based gradient descent algorithm, requiring ideal synaptic behavior of the memristive devices and complex neural circuits. To address this challenge, we demonstrate the training of a memristive restricted Boltzmann machine (memristive RBM) and deep belief neural network (memristive DBN) that employ memristor devices fabricated in a commercial complementary metal-oxide-semiconductor process as artificial synapses and utilize the gradient descent algorithm based on contrastive divergence (CD). The memristor devices are based on the floating gate (FG) principle, showing analog tunability, high endurance, long retention time, predictable cycling degradation, moderate device-to-device variations, high yield, and two orders of magnitude higher energy efficiency for multiply-accumulate operations than today's graphical processing units. The CD-based gradient descent algorithm highly relaxes both the requirements of the synaptic behavior for the memristor devices and the complexity of the neuron circuits. Two 12-by-8 arrays of FG memristors are utilized to demonstrate the training of an RBM intended for pattern recognition. We then benchmark an extrapolated memristive DBN consisting of three memristive RBMs for the MNIST dataset, showing a recognition accuracy up to 97.05%. The designed memristive RBM and DBN have minimal neuron circuits where no digital-to-analog and analog-to-digital converters are needed.

## KEYWORDS

Floating gate memristive device, hardware restricted Boltzmann machine, memristive deep belief network, contrastive divergence

## Introduction

Memristive devices, acting as artificial synapses, promise efficient and low-power brain-like neuromorphic computing. The computation is performed in the memory itself, avoiding the von Neumann bottleneck in traditional computing systems<sup>1-3</sup>. Nevertheless, there are still challenges preventing the promise from becoming a reality due to the mismatch between the memristive devices and neural network algorithms<sup>4,5</sup>.

To accelerate the training and inference of a deep neural network (DNN), ideally, multiple requirements need to be achieved by the memristive devices such as high production yield, a large number of conductance states, high uniformity, long retention times, and high endurance<sup>6-8</sup>. Emerging nonvolatile memory devices, such as resistive random-access memory (RRAM)<sup>9-12</sup>, magnetic random-access memory (MRAM)<sup>13</sup>, phase-change memory (PCM)<sup>14,15</sup>, ferroelectric memory<sup>16</sup>, and electrolyte-gated transistors<sup>17-19</sup>, have been proposed as the synaptic devices for neuromorphic computing. Notwithstanding, none of them have met all the desired requirements<sup>20</sup>. Furthermore, most of the mentioned technologies have low yield<sup>21</sup> or need special materials or processes<sup>22</sup> when being integrated into industrial complementary metal-oxide-semiconductor (CMOS) processes.

At the neural network level, error backpropagation-based gradient descent<sup>23</sup> is the golden algorithm for training a DNN. The errors are usually relatively small thus need to be handled by high precision neural circuits. Additionally, the data dependency of gradient descent on the backpropagated errors needs separated memory to store the intermediate neuron states<sup>24,25</sup>. High accuracy in the training of DNNs, paralleling that of the software counterpart, using analog memristive devices has been reported, where, however, the high precision neural circuits implemented in software<sup>26</sup>. The deep convolutional neural network (DCNN) has been implemented fully in hardware<sup>27</sup>. However, the majority weights are pre-trained on a digital computer instead of in-situ optimized using the error backpropagation algorithm, leading to extra hardware overhead. Novel network structures and training paradigms are urgently needed to enable both the efficient training and inference of a DNN in hardware.

This work investigated the two-terminal floating gate memristive synaptic devices fabricated in a standard production CMOS process flow, thus termed silicon synapses. The silicon synapses

show self-selectivity, analog conductance tunability, high retention time, small and predictable cycling degradation, and moderate device-to-device variations. The energy efficiency and performance density for multiply-accumulate (MAC) operations in an array are estimated to be  $35.6 \text{ TOPs s}^{-1}\text{W}^{-1}$  and  $6.31 \text{ TOPs s}^{-1}\text{mm}^{-2}$ , showing approximately 350 times and 170 times higher than a typical graphical processing unit (GPU). Two 12-by-8 arrays of the FG memristive devices are utilized for the in-situ training of a 19-by-8 memristive restricted Boltzmann machine (RBM) for pattern recognition via the contrastive divergence (CD) based gradient descent algorithm. The neural states are fully binarized, thus simplifying the neural circuit design where the expensive analog-to-digital and digital-to-analog converters (ADCs and DACs) are no longer needed. The prototype demonstration was extrapolated to a memristive deep belief network (DBN) consisting of three memristive RBMs for the training and recognition of the MNIST dataset. The layer-by-layer greedy learning of RBMs ensures that the weight updates only depend on local information. The performance is equivalent to the software approach and comparable to mainstream memristive DNNs based on the error backpropagation algorithm where complex neural behavior (thus peripheral circuit of the memristive array) needs to be implemented in software or hardware.

## Two-terminal floating gate memristive device

Figures 1a and 1b show the schematic diagram and scanning electron microscopy (SEM) top view of the two-terminal FG memristive device. The device consists of two parallelly connected transistors, i.e., the read transistor and the injection transistor, which share a common polysilicon floating gate (poly FG) and a drain (D). The sources of both transistors are connected externally (S). The device, i.e., the silicon synapse, is fabricated in a commercial 180nm CMOS process (Tower Semiconductor) without additional masks<sup>28,29</sup>. At positive bias ( $V_D > 0$  and  $V_S = 0$ , thus  $V_{DS} = V_D - V_S > 0$ ), the device shows non-linear current-voltage ( $I_{DS}$ - $V_{DS}$ ) relation as the combining result of the direct D-S voltage and indirect FG voltage changes (Figure 1c). The device shows negligible current at reversed voltage bias ( $V_D = 0$  and  $V_S > 0$ , thus  $V_{DS} = V_D - V_S < 0$ ) since the FG is coupled to the D, and the transistors are turned off. The non-linear I-V behavior and low reverse current endow the device with a self-selection function and lead to low sneak-path currents in crossbar arrays. Different memory states can be obtained for different amounts of the charge stored in the FG, and thus different turn-on voltages of the transistors. In this work, we use the conductance  $G$  of the device at 2V ( $G = I_R/V_R$ ,  $V_R = 2\text{V}$ ) to denote the state of the memristive device.

The silicon synapse can be depressed (programmed) or potentiated (erased) by applying a voltage pulse on the D or S terminal, which will inject electrons and holes into the FG<sup>30-32</sup>, respectively (see Methods and Extended Data Fig. 1). Analog conductance tunability can be obtained

by using depression or potentiation pulses with a width of  $10\ \mu\text{s}$  (Extended Data Fig. 2). The conductance states are nonvolatile (Extended Data Fig. 3). The depression and potentiation cycling test is performed by alternatively depressing and potentiating the device between the high conductance state (HCS,  $\sim 1\ \mu\text{S}$ ) and the low conductance state (LCS,  $\sim 1\ \text{nS}$ ). One loop of switching from the HCS to LCS and backward to HCS is defined as one test cycle. Up to 400 reliable test cycles have been measured with more than 53,000 writing pulses (Figure 1d), which shows small degradations as the later cycles need more pulses to switch between HCS and LCS (Extended Data Fig. 4). A physical-based model has been developed to simulate the switching behavior, including cycling degradation<sup>33</sup> (see Methods, Extended Data Fig. 1 and Extended Data Fig. 4). For digital switching (between HCS and LCS only), the endurance can be more than  $10^5$  cycles<sup>30</sup>.

To confirm the long-term retention in the analog switching, 16 devices are written to 16 evenly spaced conductance levels in logarithmic scale between the LCS and HCS and monitored for more than two months at room temperature (Figure 1e). The LCS experiences small shifts, but none of the states are overlapping. The retention of analog conductance is projected to be higher than ten years, as indicated by the dashed lines in Figure 1e.

### **Memristive synaptic array.**

The silicon synapses are integrated into a crossbar array, accommodating 12-by-8 (thus 96 in total) memristors in a single chip (Figure 2a-2c). A test system, consisting of a customized PCB board, an FPGA evaluation board, and a B1500 semiconductor analyzer, is developed to enable individual memristors' reads, potentiations, and depressions in two 12-by-8 arrays (two chips, see Extended Data Fig. 5). The weighted summation of synapses in a neural network is physically embodied by the vector-matrix multiplications (VMM) using the silicon synapse array. The conductance of each of the synaptic devices can be configured by potentiation and depression pulses (see Methods and Extended Data Fig. 6). As illustrated in Figure 2d, we can see that there is no write or read disturbs over other devices in the array when operating a single device. The device-to-device variations are measured by fully depressing and potentiating all cells in the array between HCS and LCS (Figure 2e-2f and Extended Data Fig. 7). Pixelated letters and digits of “TECHNION” and “asic2lab” are written into the two chips (192 devices in total), as shown in Figure 2g, to verify the conductance tunability and memory function. All devices we have measured are working well, demonstrating 100% yield. For the multiply-accumulate (MAC) operations in an array, the computational efficiency is estimated to be  $3.56 \times 10^4$  GOPs  $\text{s}^{-1}\text{W}^{-1}$  energy and  $6.31 \times 10^3$  GOPs  $\text{s}^{-1}\text{mm}^{-2}$  in area, which are approximately 350 times and 170 times improvement on energy efficiency and performance density, respectively, compared with Tesla V100 GPU in 12 nm technology (see Methods)<sup>26</sup>.

Two remaining non-idealities of the synapses are the non-ohmic current-voltage (I-V) reading behavior and the non-linear conductance update for increasing potentiation or depression stimuli. These issues are also faced by other types of memristive synaptic devices, hindering the hardware implementation of DNN in simple and straightforward ways<sup>34</sup>. The non-ohmic issue prevents the analog multiplication using Ohm’s law, which can be solved by using pulse number or pulse width modulated input signals to represent analog inputs<sup>35,36</sup>. The non-linear conductance update behavior refers to the fact that the change of conductance or weight per pulse depends on the current conductance or weight of the synapse synapses<sup>37,38</sup>. As a result, iterative write-and-verify operation<sup>27,39</sup> is needed to ensure the synaptic weight is correctly written to the target for each training batch. These solutions incur large hardware and latency overheads of the DNN in both inference and training stages.

Unlike the mainstream DNN, we demonstrate the memristive DBN consisting of stacked memristive RBM layers. The inherent binary neuron states obviate the non-ohmic reading issues since only a fixed read voltage is needed. The memristive RBM and DBN utilize a modified CD learning algorithm that separates the synaptic weighted summation from the accumulation of weight update requests, simultaneously solving the non-linear weight update issue.

### Training of the memristive RBM

We train a memristive RBM using two-terminal floating gate memristive devices as synaptic connections. Figure 3a shows the structure of the RBM, which has 19 visible units and 8 hidden units. The 19 visible units are partitioned into two parts: 12 for the pixel inputs of 4-by-3 pixelated letters or digits and 7 for the label inputs. Seven black-and-white patterns, each having 4-by-3 binary pixels (‘1’ for black pixels, and ‘0’ for white pixels) denoting letters “A”, “B”, “C”, “X”, “Y”, “0”, and “1”, are used as inputs (Figure 3b), and their labels are presented in by one-hot vectors (for instance, the label for “A” has the code of “1000000”). The weight matrix between visible units and hidden units is thus partitioned into two sub-matrices:  $\mathbf{w}_1$  of the size 12-by-8 and  $\mathbf{w}_2$  of the size 7-by-8, which are implemented by two memristive device arrays ( $\mathbf{G}_1$  and  $\mathbf{G}_2$ ) in the two chips of our measurement system, as shown in Figure 3c.

The details of the training procedure of the memristive RBM are described in the Methods and Extended Data Fig. 8. The VMM and stochastic sampling are performed *in-situ* in the memristive device array with the help of externally injected noise currents<sup>40</sup> (Figure 3d). The inputs of the VMM and the stochastic sampling outputs are binary, thus no high precision digital-to-analog or analog-to-digital converters are required. Forward VMM and sampling hidden units upon visible units, as well as backward VMM and sampling visible units upon the hidden units, are alternately performed, which

gives the visible unit states  $\mathbf{v}$  (i.e., the input), the hidden unit states  $\mathbf{h}$ , the reconstructed visible unit states  $\mathbf{v}'$ , and the reconstructed hidden unit states  $\mathbf{h}'$ . The contrastive divergence (CD) between the initial visible-hidden unit pairs and the reconstructed visible-hidden unit pairs, that is,  $\mathbf{v}\mathbf{h}^T - \mathbf{v}'\mathbf{h}'^T$ , provides the descendent gradient of weight updates, that is,  $\Delta\mathbf{w} \sim (\mathbf{v}\mathbf{h}^T - \mathbf{v}'\mathbf{h}'^T)$ , to minimize the energy of the RBM and improve the recognition accuracy in the inference stage.

The CD has only ternary elements (-1, 0, or 1) since all the neuron unit states are binary. The CD elements are then accumulated in a digital counter array to avoid writing the device in every training sample input (Figure 3e). After the accumulated CD element reaches a positive or negative threshold (+5 or -5 for the presented experiment), potentiation or depression pulses are sent to the memristive device to update the weights, respectively. The blind write method is used, which means that the updated weights do not need to be verified or fine-tuned, making programming fast and affordable. The memristive RBM is trained for 200 epochs, and each epoch comprises the 7 patterns and their labels, i.e., 7 training samples. Figures 3f and 3g show three representative traces of the accumulated CD and conductance of corresponding memristive devices, respectively, as a function of the number of training samples. It can be seen that most of the consecutive weight updates cancel each other, leading to infrequent memristive device writing. Figure 3h shows the conductance evolutions of all the devices in the two arrays during the training. The success of the training is reflected by the reduction of reconstruction error of the visible unit states ( $\langle \mathbf{v} - \mathbf{v}' \rangle$ ) (Figure 3i) and the increase of the recognition accuracy for all 7 learned patterns (Figure 3j), as a function of the training epoch.

### Training of the memristive DBN

The single memristive RBM is extrapolated to memristive DBN consisting of three RBMs with the sizes of (784-500, 500-500, (500+10)-2000) stacking on each other (Figure 4a and Methods). The handwritten digits of the MNIST dataset<sup>41</sup> are used for training. Greedy learning algorithm<sup>42</sup> is employed here: we first train the RBM-1 layer using the digit images as input, followed by training the RBM-2 and RBM-3 layer sequentially using the hidden unit states of the previous layer and labels (last layer only) as input. The reconstruction errors for each RBM layer are shown in Figure 4b, revealing apparent reduction and convergence of the reconstruction error. The image recognition, i.e., the inference of the neural network, can be conducted by expanding the RBM-3 layer, i.e., processing the image by the path  $\mathbf{w}_1 \rightarrow \mathbf{w}_2 \rightarrow \mathbf{w}_3 \rightarrow \mathbf{w}_4$ . Since each RBM layer is designed to have a stochastic binarized output for the training, the test accuracy has a probabilistic distribution. The stochasticity can be eliminated by removing the noise current injection to speed up testing in Figure 3d, such that the inference is *deterministic*. Another way is to repeat the stochastic inference and take the average

(*sampling inference*). Figure 4c shows the test accuracy of the test set images in the MNIST dataset during the training of the memristive DBN for both deterministic inference and 50-time sampling inference. The first 30 epochs are in the phase of the training of the RBM-3, and the last 30 epochs are in the phase of fine-tuning the memristive DBN by the wake-sleep algorithm<sup>43</sup> under the same hardware design (see Methods). The accuracy of deterministic inference after the 60-epoch training is 95.67%, while the 50-time sampling inference gives an accuracy of 97.05%, which are 2.63% and 1.25% lower than the DBN trained in software (98.3%), respectively. The accuracy for the 50-time sampling inference (Samp. #50) is comparable to recently reported DNN based on PCM<sup>26,44</sup> and RRAM<sup>27</sup> devices where the peripheral circuit to realize the neural activities are much more complex to be realized in hardware, as summarized in Figure 4d.

## Conclusion

The fully CMOS-compatible silicon synapse based on two-terminal floating memristive devices experimentally manifests a spectrum of advantages in serving the role of an artificial synapse, including self-selection, analog conductance tunability, reliable cycling behavior, high yield, moderate device-to-device variation, predictable cycle to cycle degradation, and low energy consumption. The training and inference of memristive RBM are demonstrated using the developed silicon synapses. The memristive RBM features binary neurons, thus resolving the non-Ohmic I-V issue and significantly reducing the complexity of the peripheral (neural) circuit. Utilizing the CD-based gradient descent learning algorithm, the calculation and accumulation of the weight update requests were separated from VMM and sampling operations in RBM in a mixed-signal learning scheme, making the training highly immune to the non-linear weight update behavior. The number of write operations, hence the endurance requirement of the memristor device, is significantly reduced. The memristive RBM is then extrapolated to DBN, which shows performance comparable to that of the software and the state-of-the-art memristive DNNs, which need much more complex neural circuits.

## REFERENCES

1. Ielmini, D. & Wong, H.-S. P. In-memory computing with resistive switching devices. *Nat. Electron.* **1**, 333–343 (2018).
2. Fuller, E. J. *et al.* Parallel programming of an ionic floating-gate memory array for scalable neuromorphic computing. *Science* (80-. ). **364**, 570–574 (2019).
3. Chen, W.-H. *et al.* CMOS-integrated memristive non-volatile computing-in-memory for AI edge processors. *Nat. Electron.* **2**, 420–428 (2019).

4. Wang, W. *et al.* Integration and Co-design of Memristive Devices and Algorithms for Artificial Intelligence. *iScience* **23**, 101809 (2020).
5. Zidan, M. A., Strachan, J. P. & Lu, W. D. The future of electronics based on memristive systems. *Nat. Electron.* **1**, 22–29 (2018).
6. Gokmen, T. & Vlasov, Y. Acceleration of Deep Neural Network Training with Resistive Cross-Point Devices: Design Considerations. *Front. Neurosci.* **10**, 333 (2016).
7. Cheng, H. Y. *et al.* An ultra high endurance and thermally stable selector based on TeAsGeSiSe chalcogenides compatible with BEOL IC Integration for cross-point PCM. in *2017 IEEE International Electron Devices Meeting (IEDM) 2.2.1-2.2.4* (IEEE, 2017). doi:10.1109/IEDM.2017.8268310.
8. Chang, C. C. *et al.* Mitigating Asymmetric Nonlinear Weight Update Effects in Hardware Neural Network Based on Analog Resistive Synapse. *IEEE J. Emerg. Sel. Top. Circuits Syst.* **8**, 116–124 (2018).
9. Wang, C. *et al.* Scalable massively parallel computing using continuous-time data representation in nanoscale crossbar array. *Nat. Nanotechnol.* (2021) doi:10.1038/s41565-021-00943-y.
10. Li, C. *et al.* Long short-term memory networks in memristor crossbar arrays. *Nat. Mach. Intell.* **1**, 49–57 (2019).
11. Wang, Z. *et al.* In situ training of feed-forward and recurrent convolutional memristor networks. *Nat. Mach. Intell.* **1**, 434–442 (2019).
12. Wang, W. *et al.* Learning of spatiotemporal patterns in a spiking neural network with resistive switching synapses. *Sci. Adv.* **4**, eaat4752 (2018).
13. Romera, M. *et al.* Vowel recognition with four coupled spin-torque nano-oscillators. *Nature* **563**, 230–234 (2018).
14. Boybat, I. *et al.* Neuromorphic computing with multi-memristive synapses. *Nat. Commun.* **9**, 2514 (2018).
15. Sebastian, A. *et al.* Temporal correlation detection using computational phase-change memory. *Nat. Commun.* **8**, 1115 (2017).
16. Ni, K. *et al.* Ferroelectric ternary content-addressable memory for one-shot learning. *Nat. Electron.* **2**, 521–529 (2019).
17. van de Burgt, Y., Melianas, A., Keene, S. T., Malliaras, G. & Salleo, A. Organic electronics for neuromorphic computing. *Nat. Electron.* **1**, 386–397 (2018).
18. Chien, N. A. *et al.* Synergistic Gating of Electro-Iono-Photoactive 2D Chalcogenide Neuristors: Coexistence of Hebbian and Homeostatic Synaptic Metaplasticity. *Adv. Mater.*



**30**, 1800220 (2018).

19. Yang, J. *et al.* Artificial Synapses Emulated by an Electrolyte-Gated Tungsten-Oxide Transistor. *Adv. Mater.* 1801548 (2018) doi:10.1002/adma.201801548.
20. Wang, Z. *et al.* Resistive switching materials for information processing. *Nat. Rev. Mater.* **5**, 173–195 (2020).
21. Lee, S., Sohn, J., Jiang, Z., Chen, H.-Y. & Philip Wong, H.-S. Metal oxide-resistive memory using graphene-edge electrodes. *Nat. Commun.* **6**, 8407 (2015).
22. Xia, Q. & Yang, J. J. Memristive crossbar arrays for brain-inspired computing. *Nat. Mater.* **18**, 309–323 (2019).
23. LeCun, Y., Bengio, Y. & Hinton, G. Deep learning. *Nature* **521**, 436–444 (2015).
24. Song, L., Qian, X., Li, H. & Chen, Y. PipeLayer: A Pipelined ReRAM-Based Accelerator for Deep Learning. in *2017 IEEE International Symposium on High Performance Computer Architecture (HPCA)* 541–552 (IEEE, 2017). doi:10.1109/HPCA.2017.55.
25. Shafiee, A. *et al.* ISAAC: A Convolutional Neural Network Accelerator with In-Situ Analog Arithmetic in Crossbars. in *Annual International Symposium on Computer Architecture (ISCA)* 14–26 (IEEE, 2016). doi:10.1109/ISCA.2016.12.
26. Ambrogio, S. *et al.* Equivalent-accuracy accelerated neural- network training using analogue memory. *Nature* **558**, 60–67 (2018).
27. Yao, P. *et al.* Fully hardware-implemented memristor convolutional neural network. *Nature* **577**, 641–646 (2020).
28. Danial, L. *et al.* Two-terminal floating-gate transistors with a low-power memristive operation mode for analogue neuromorphic computing. *Nat. Electron.* **2**, 596–605 (2019).
29. Roizin, Y. & Pikhay, E. Memristor using parallel asymmetrical transistors having shared floating gate and diode. *US Pat.* US9514818B1 (2016).
30. Pavan, P., Bez, R., Olivo, P. & Zanoni, E. Flash memory cells-an overview. *Proc. IEEE* **85**, 1248–1271 (1997).
31. Diorio, C., Hasler, P. & Minch, B. A. A single-transistor silicon synapse. *IEEE Trans. Electron Devices* **43**, 1972–1980 (1996).
32. Ziegler, M., Oberländer, M., Schroeder, D., Krautschneider, W. H. & Kohlstedt, H. Memristive operation mode of floating gate transistors: A two-terminal MemFlash-cell. *Appl. Phys. Lett.* **101**, (2012).
33. Wang, W. *et al.* Physical based compact model of Y-Flash memristor for neuromorphic computation. *Appl. Phys. Lett.* **119**, 263504 (2021).
34. Ielmini, D. & Pedretti, G. Device and Circuit Architectures for In-Memory Computing. *Adv.*

*Intell. Syst.* **2**, 2000040 (2020).

35. Yao, P. *et al.* Face classification using electronic synapses. *Nat. Commun.* **8**, 15199 (2017).
36. Cai, F. *et al.* A fully integrated reprogrammable memristor–CMOS system for efficient multiply–accumulate operations. *Nat. Electron.* **2**, 290–299 (2019).
37. Jang, J.-W., Park, S., Burr, G. W., Hwang, H. & Jeong, Y.-H. Optimization of Conductance Change in  $\text{Pr}_{1-x}\text{Ca}_x\text{MnO}_3$ -Based Synaptic Devices for Neuromorphic Systems. *IEEE Electron Device Lett.* **36**, 457–459 (2015).
38. Burr, G. W. *et al.* Experimental Demonstration and Tolerancing of a Large-Scale Neural Network (165 000 Synapses) Using Phase-Change Memory as the Synaptic Weight Element. *IEEE Trans. Electron Devices* **62**, 3498–3507 (2015).
39. Milo, V. *et al.* Accurate Program/Verify Schemes of Resistive Switching Memory (RRAM) for In-Memory Neural Network Circuits. *IEEE Trans. Electron Devices* 1–6 (2021) doi:10.1109/TED.2021.3089995.
40. Mahmoodi, M. R., Prezioso, M. & Strukov, D. B. Versatile stochastic dot product circuits based on nonvolatile memories for high performance neurocomputing and neurooptimization. *Nat. Commun.* **10**, 5113 (2019).
41. Lecun, Y., Bottou, L., Bengio, Y. & Haffner, P. Gradient-based learning applied to document recognition. *Proc. IEEE* **86**, 2278–2324 (1998).
42. Hinton, G. E., Osindero, S. & Teh, Y.-W. A Fast Learning Algorithm for Deep Belief Nets. *Neural Comput.* **18**, 1527–1554 (2006).
43. Hinton, G., Dayan, P., Frey, B. & Neal, R. The ‘wake-sleep’ algorithm for unsupervised neural networks. *Science (80-. )*. **268**, 1158–1161 (1995).
44. Nandakumar, S. R. *et al.* Mixed-precision architecture based on computational memory for training deep neural networks. in *International Symposium on Circuits and Systems (ISCAS)* (2018).
45. Nandakumar, S. R. *et al.* Mixed-Precision Deep Learning Based on Computational Memory. *Front. Neurosci.* **14**, 1–16 (2020).
46. Simon Tam, Ping-Keung Ko & Chenming Hu. Lucky-electron model of channel hot-electron injection in MOSFET’S. *IEEE Trans. Electron Devices* **31**, 1116–1125 (1984).
47. Yoshikawa, K. *et al.* Lucky-hole injection induced by band-to-band tunneling leakage in stacked gate transistors. in *Technical Digest - International Electron Devices Meeting* vol. 53 577–580 (1990).
48. Ielmini, D., Ghetti, A., Spinelli, A. S. & Visconti, A. A study of hot-hole injection during programming drain disturb in flash memories. *IEEE Trans. Electron Devices* **53**, 668–676

(2006).

## **ACKNOWLEDGMENTS**

This work was supported by the European Research Council through the European Union's Horizon 2020 Research and Innovation Programme under Grant 757259 and FET-Open NeuChip project under grant agreement No. 964877. W.W. was supported in part at the Technion by the Aly Kaufman Fellowship. W.W. acknowledges the help from Devangshu Dutta on the PCB and FPGA code development.

## **AUTHOR CONTRIBUTIONS**

W.W. conceived the concept of Y-Flash memristor-based RBM and DBN, L.D. designed the memristive chip and led tapeout to fabrication, including array layout and readout cells and developed device level operation schemes, Y.R. and E.P. suggested the Y-Flash memristor cell and performed initial verification, W.W. conducted the device characterization, array level operation schemes with the assistance of L.D., E.H. and B.H. W.W. conducted neural network demonstration, and simulations with the assistance of L.D. and Y.L. Y.R., E.P. and Z.W. helped the illustration results. All of the authors discussed the results and contributed to the preparation of the manuscript. S.K. supervised the research.

## **ADDITIONAL INFORMATION**

**Supplementary information** accompanies this paper at <http://www.xxx//>

**Competing financial interests:** The authors declare no competing interests.

## FIGURES AND FIGURE CAPTIONS

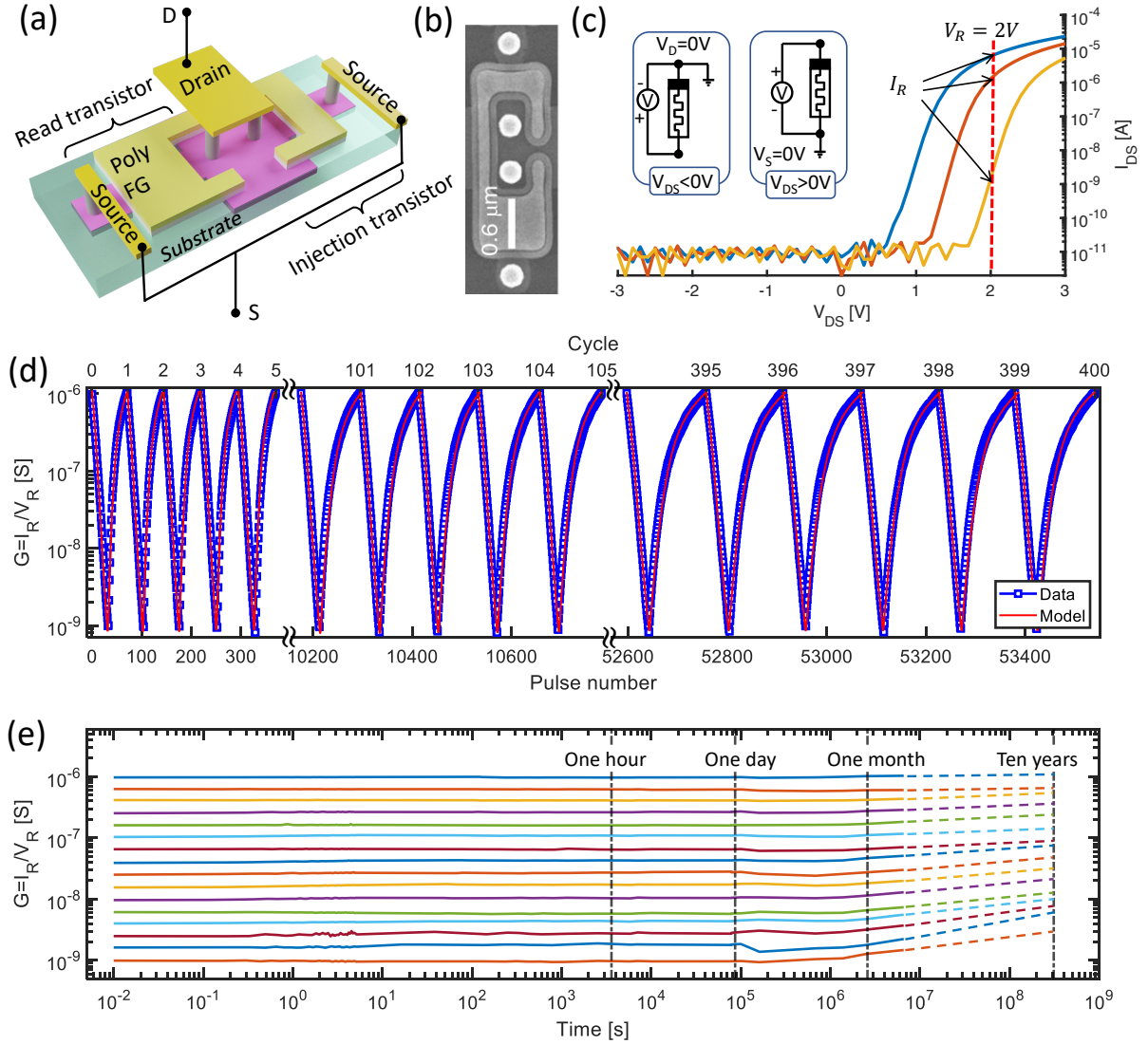


**Figure 1 | Memristive synapse based on two-terminal floating gate devices.** (a) Illustration of the floating gate devices featuring parallel connection of two transistors with a common floating gate and a common drain. The two sources are connected to form a two-terminal configuration. (b) Scanning electron microscopy (SEM) image of the fabricated device. (c) The low voltage sweep reading of the devices shows high self-selection ability. The states (different colored lines) of the device are defined by the current ( $I_R$ ) at positive bias ( $V_R=2V$ ). Inset: schematics of the negative and positive bias reading configurations (the I-V curves are measured in the two configurations separately and concatenated in the main graph). (d) Write cycling of the device. The device is alternatively depressed and potentiated between the high conductance state (HCS) and the low conductance state (LCS) for 400 test cycles (see Methods, Extended Data Fig. 2, and Extended Data Fig. 3 for the details of the write operations). A compact model is developed to accurately describe the conductance switching and cycling degradation (Methods and Extended Data Fig. 4). (e) Retention of 16 conductance levels of the devices measured for more than one month at room temperature and projected to 10 years.

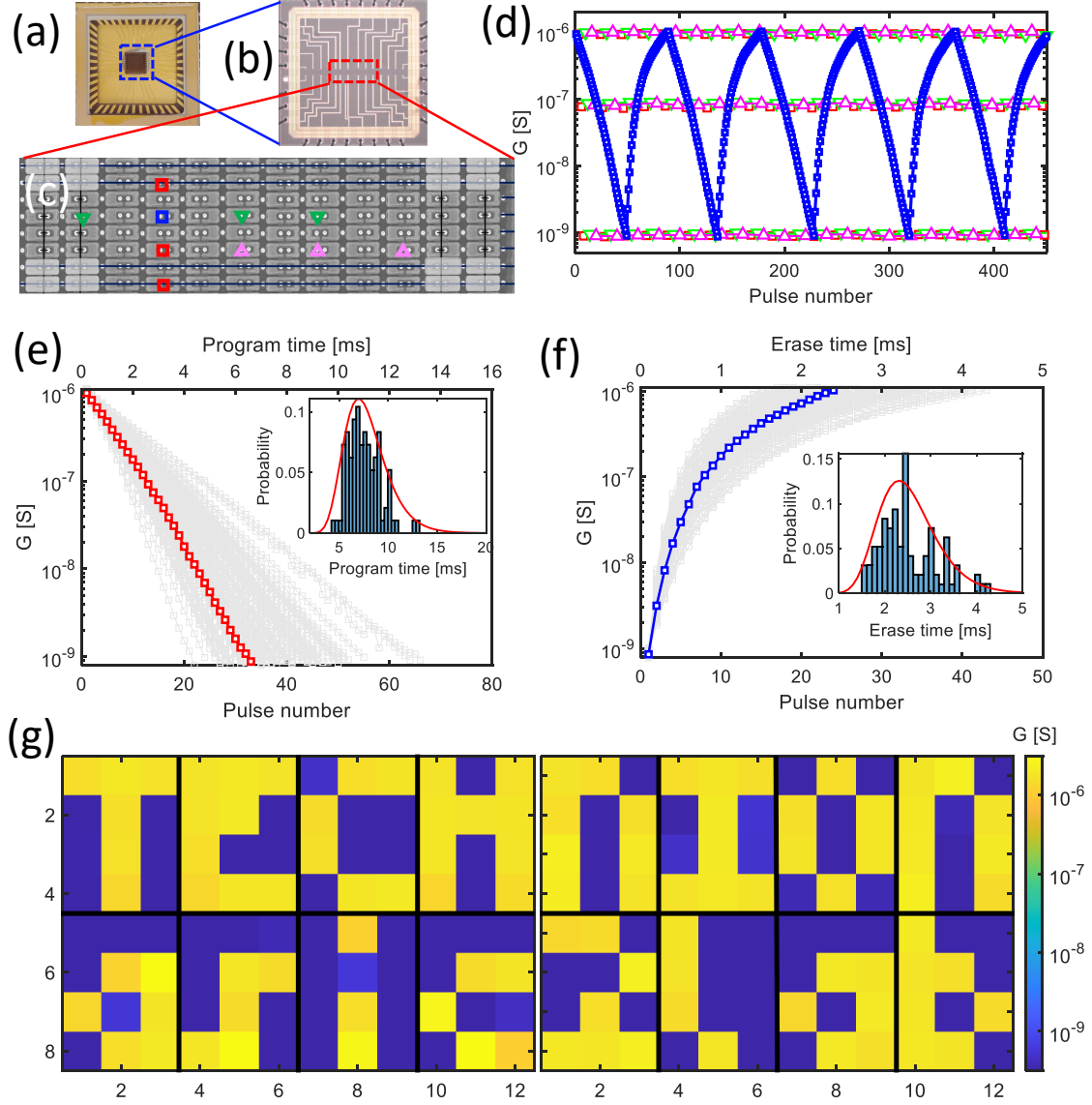


**Figure 2 | Memristive synaptic array and device-to-device variations.** Images of (a) the packaged chip and a (b) 12x8 size array design. (c) SEM image of the 12x8 array. (d) Write disturb of silicon synapses in the same array when writing to a single selected device (device locations are indicated in c). (e) Depression behavior of all the 96 devices in an array. (f) Potentiation behavior of all the 96 devices in an array. Insets of (e) and (f): statistical results of the full program time from HCS to LCS and the full erase time from LCS to HCS, respectively. The model well captures the device-to-device variation (see Methods and Extended Data Fig. 7). (g) Demonstration of the memory function by writing patterns of letters and digits (“TECHNION” and “asic2lab”) into two 12x8 memristive arrays.

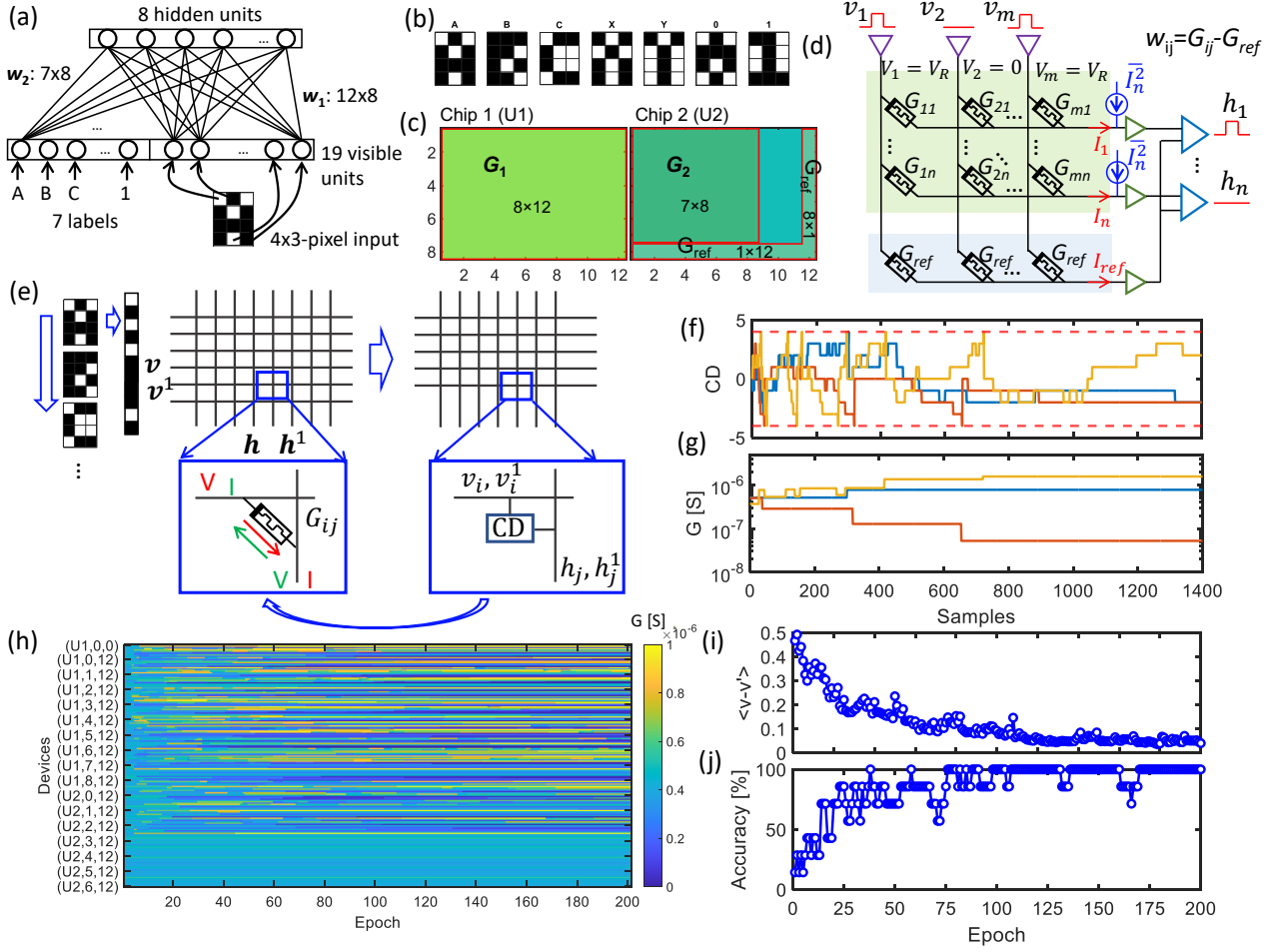


**Figure 3 | Demonstration of the restricted Boltzmann machine (RBM) training using two memristive synaptic chips.** (a) The RBM structure for demonstration with 19 visible units (12 for the pixels of input images and 7 for labels) and 8 hidden units. (b) Images of 7 image patterns of 4x3 size for the training. (c) Allocation of the weight matrix on the two memristive synaptic chips. (d) Schematic illustration of performing vector-matrix multiplications and stochastic sampling (sampling VMM) within the synaptic arrays. (e) Schematic of the mixed-signal training of an RBM by separating the sampling VMM and gradient accumulation. Detailed evolutions of (f) the accumulation of contrastive divergence (CD) and (g) the conductance of the synaptic device during the training. (h) Conductance evolution of all synaptic devices during the training. (i) The reconstruction error of RBM as a function of the training epoch. (j) Test accuracy as a function of the training epoch.

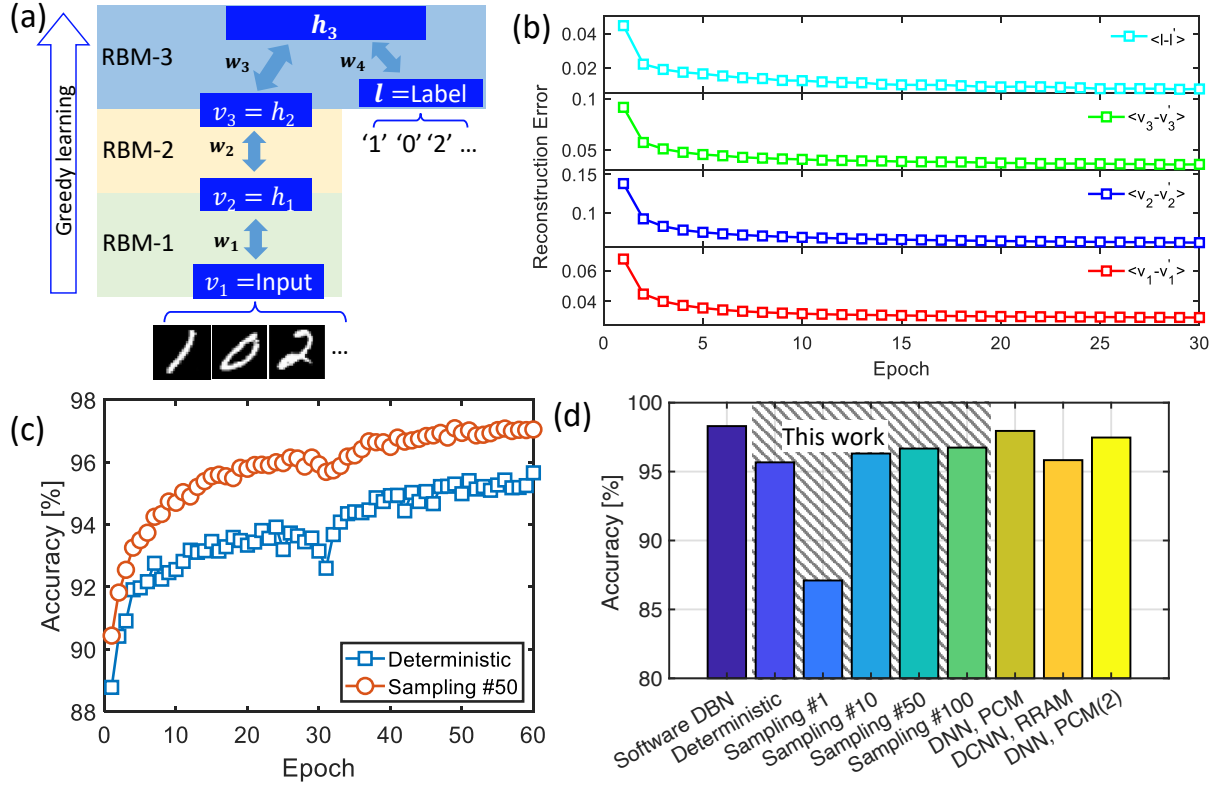


**Figure 4 | Training of the deep belief net based on the silicon synapses for MNIST dataset.** (a) Structure of the deep belief net consisting of stacked RBMs. (b) The reconstruction errors of the visible units in the three RBMs as a function of the training epoch. (c) Test accuracy of the neural network as a function of training epoch for deterministic inference and sampling inference of 50 times repetition. (d) Comparison of the test accuracy of the floating gate memristive device-based deep belief net with the software solution and other memristive deep neural networks [DNN-PCM<sup>26</sup>, DCNN-RRAM<sup>27</sup>, DNN-PCM(2)<sup>45</sup>].

## METHODS

**Device fabrication and characterization.** The memristive devices were fabricated in Tower Semiconductor's 180nm/5V CMOS process (gate oxide thickness 110 Å). Each device consists of two NMOS transistors: the readout transistor and the injection transistor (Figure 1a-1b, and Extended Data Fig. 1a), sharing a common floating gate using the polysilicon layer – the normal gate layer for CMOS transistors. The FG is surrounded by high-quality dielectrics, ensuring high retention of the charge stored in the FG. No additional masks are needed for the fabrication compared with the standard CMOS process. The injection transistor has a shorter channel (0.3  $\mu\text{m}$ ) and an additional p-type implant in the drain junction (compared with standard NMOS transistors), optimized to enhance the hot carrier injection. The read transistor (channel length 0.6  $\mu\text{m}$ ) has a lower threshold voltage to enhance the read current. The device structure was originally developed as an embedded digital nonvolatile memory (NVM), named as Y-Flash memory<sup>29</sup>, and is widely used by Tower Semiconductor foundry customers.

For single device measurement, the DC sweeping measurement and pulse-induced switching characteristics of the device were conducted by probing the device using Cascade 12000 probe station and collecting the data using a B1500 Semiconductor Analyzer. The source measurement unit (SMU) module of B1500 is used to conduct the DC sweeping measurement, and the waveform generator/fast measurement unit (WGFMU) is used to provide the pulse with accurate pulse width and amplitude for potentiation and depression operations. The substrate of the device is consistently grounded. The device should always be operated with positive voltages since a negative voltage on the drain or source terminals of the transistors will induce unexpected large current from the ground due to the positive bias of the p-n junctions between the p-type substrate and n-type ohmic contacts of the drain/source terminals (Extended Data Fig. 1a). The sources of the readout transistor (Source Read, SR) and the injection transistor (Source Injection, SI) are shortened externally (Extended Data Fig. 1a). Thus, the device acts as a two-terminal memristive device (Extended Data Fig. 1b).

**Readout, depression, and potentiation.** The readout operation is conducted by applying a voltage pulse (amplitude  $V_R=2\text{V}$ ) and sensing the current ( $I_R$ ), as shown in Extended Data Fig. 2a. The state of the device is denoted by the conductance  $G=I_R/V_R$ .

The depression of the memristive device corresponds to the program operation of the conventional floating gate device. It is conducted by applying a high voltage pulse on the drain terminal and grounding the source terminal (Extended Data Fig. 2b). We used a fixed amplitude of  $V_P=5\text{V}$  for the depression/program operations. The potentiation of the memristive device corresponds to erase operation. It is conducted by applying a high voltage pulse on the source terminal and



grounding or floating the drain terminal (Extended Data Fig. 2c). The fixed amplitude of  $V_E=8V$  is used for the potentiation/erase operations.

The pulse-induced depression is performed by alternatively applying the program pulse and readout pulse, as shown in Extended Data Fig. 2d. When program pulses have a short pulse width (10 us), we can obtain more than 1500 conductance states between HCS and LCS (Extended Data Fig. 2e), showing an analog type switching behavior. The pulse-induced potentiation is performed by alternatively applying the erase pulse and readout pulse, as shown in Extended Data Fig. 2d. Similar to the depression, when the erase pulses have a short pulse width (10 us, Extended Data Fig. 2f), we can obtain analog-type behavior with more than 800 conductance states from LCS to HCS (Extended Data Fig. 2g).

Varying the pulse width for the depression and potentiation operations trades off between a higher number of conductance states and a larger conductance change stride. We chose the pulse width for the depression and potentiation to be 200 us and 100 us to character the device and for tuning the conductance for neural network learning. The typical pulse-induced depression and potentiation curves are shown in Extended Data Fig. 3a and Extended Data Fig. 3b, respectively. We continuously read the device for all intermediate states for 20 seconds, and all the states are stable and show negligible read noise (Extended Data Fig. 3c and Extended Data Fig. 3d).

**Operation mechanisms and device modeling.** To model the I-V characteristics of the device, we first need to obtain the floating gate voltage ( $V_{FG}$ ). The coupling capacitor net determines the floating gate voltage between the device's floating gated and other terminals and the charge  $Q_{FG}$  at the floating gate. The floating gate voltage can be written as:

$$V_{FG} = \frac{Q_{FG} + C_{GD}V_D + (C_{GSR} + C_{GSI})V_S}{C_{GSR} + C_{GD} + C_{GSI} + C_{GB}} \approx \frac{Q_{FG} + C_{GD}V_D}{C_{GSR} + C_{GD} + C_{GSI} + C_{GB}}, \quad (1)$$

where  $C_{GSR}$ ,  $C_{GD}$ ,  $C_{GSI}$ , and  $C_{GB}$  are the capacitance between the floating gate and SR, the floating gate and D, the FG and SI, the FG and substrate, respectively, as shown in Extended Data Fig. 1a.  $V_D$  and  $V_S$  are the voltages applied on the D and S terminals, respectively. Notice that the capacitance between the floating gate and the D ( $C_{GD}$ ) is much higher than other capacitances<sup>26</sup>. For positive bias of the device ( $V_D > 0$ ,  $V_S = 0$ ),  $V_{FG}$  linearly increases with  $V_D$  and the transistors will be gradually opened (Extended Data Fig. 1c). The current of the device can be obtained by determining the D-to-S current of both the readout transistor and injection transistor in both the sub-threshold and above-threshold regions. For reversed bias of the device ( $V_D = 0$ ,  $V_S > 0$ , thus  $V_{DS} = V_D - V_S < 0$ ),  $V_{FG}$  is defined primarily by drain voltage. The transistors will remain closed, and the device shows a low readout current.

A high D-to-S current is expected when a higher voltage is applied to the D and the S is

grounded. In the injection transistor with a short channel, the high SI-to-D electrical field accelerates the electrons. A small number of accelerated electrons (hot electrons) will be injected into the floating gate, i.e., channel hot electron injection (CHEI), as shown in Extended Data Fig. 1d. The process is similar to the program operation in conventional FG devices<sup>31,46</sup>. The induced gate current can be written as

$$I_{G,program} = -I_{DS}P_0e^{-\frac{V_\alpha}{V_{FG}}}, \quad (2)$$

where  $I_{DS}$  is the D-to-S current of the injection transistor,  $P_0$  is the probability of the hot electrons to be emitted into the floating gate, and  $V_\alpha$  is a fitting parameter. The electron injections to the floating gate will decrease the total charge on the floating gate. Thus, the floating gate voltage is decreased for a particular read voltage bias. The readout current and the conductance of the device are decreased, corresponding to the depression of the synaptic weight.

The drain-source current is negligible when a higher voltage is applied to the S, and the D is grounded or floating. However, the barrier between the channel and the source in the injection transistor is reversely biased, which will induce the band-to-band hole generation in the drain region of the transistor. The high source-to-drain electrical field accelerates the generated holes, and the lucky ones are injected into the floating gate (Extended Data Fig. 1d). The hot hole gate current can be written as<sup>47,48</sup>

$$I_{G,erase} = \xi(V_{FG} - V_{bi})^2e^{-\frac{\beta}{V_{FG}-V_{bi}}}, \quad (3)$$

where  $\xi$  and  $\beta$  are the fitting parameters reflecting the hole injection efficiency, and  $V_{bi}$  is the channel potential in the injection site, where the injection of holes takes place. This process decreases the total charge on the floating gate and increases the conductance of the device, corresponding to the potentiation of the synaptic weight.

The cycling degradation of the device is modeled by adding the degradation features to the parameters controlling the efficiency of electron or hole injections in the program and erase operations, i.e.,  $V_\alpha$  and  $\beta$ , respectively. The degradations of these two parameters are written as

$$\frac{dV_\alpha}{dt_{prog}} = (V_{\alpha,max} - V_\alpha)(e^{\frac{t_{prog}}{\tau_{prog}}} - 1), \quad (3)$$

and

$$\frac{d\beta}{dt_{erase}} = (\beta_{max} - \beta)(e^{\frac{t_{erase}}{\tau_{erase}}} - 1), \quad (4)$$

where  $t_{prog}$  and  $t_{erase}$  are the total time of the program or erase operations applied to the device,  $V_{\alpha,max}$  and  $\beta_{max}$  are the stable values of these parameters after operating for a long time,  $\tau_{prog}$  and  $\tau_{erase}$  are the time constants of the degradation.

The increase of the full depression/program time and full potentiation/erase times as the

function of the number of the cycles is shown in Extended Data Fig. 4, which shows good agreement between the data and the model. The simulated depression and potentiation curves match the experimental data well, as shown in Fig. 1d.

The device-to-device variation is modeled by adding a Gaussian-type variation to the parameters in the exponents of the gate current for the program and erase operations, that is,  $V_{\alpha,d2d} \in \mathcal{N}(V_{\alpha}, \sigma_{V_{\alpha}}^2)$  and  $\beta_{d2d} \in \mathcal{N}(\beta, \sigma_{\beta}^2)$ , where  $\sigma_{V_{\alpha}}$  and  $\sigma_{\beta}$  are the standard variations of the parameters  $V_{\alpha}$  and  $\beta$ . The values of the parameter  $V_{\alpha}$  and  $\beta$  for each device are randomly chosen from the distributions at the initial stage. The simulated program and erase traces, including device-to-device variations, are shown in Extended Data Fig. 7, which well reproduces the measure device-to-device variation in Fig. 2e and Fig. 2f.

**Testing system.** To enable the investigation of device operation within an array, device-to-device variations, and demonstration of the training and inference of a memristive RBM layer, a test system which integrates two Y-Flash chips, each containing a 12-by-8 memristive device array, is developed and presented in Extended Data Fig. 5. The system consists of a custom printed circuit board (PCB, a Z702 FPGA development board, a B1500 semiconductor analyzer, a controlling personal computer (PC), and power supplies.

In the custom PCB board, we use cross-point switch array (AD75019) chips to route all the terminals of the two Y-Flash chips to four channels of the B1500 SMUs/WGFMUs. The FPGA configures the cross-point switching array chips such that SMUs/WGFMUs can be arbitrarily connected to each terminal of the memristive device array. The WGFMUs provide the pulses for readout, potentiation, and depression operations and sense the current in the readout mode. The SMUs in B1500 provide voltage biases for different operation modes. The FPGA board and the B1500 are controlled by a PC to synchronize the connections and the pulse applying/sensing operations.

**Array operations.** The read operation of a single device can be performed by applying a read voltage on the D and grounding the S of the target device, and floating all other terminals in the array. The low conductance of the device at reversed bias in Figure 1c provides the self-selection functionality and guarantees that there are no detectable sneak path currents.

The forward VMM is conducted in the array by applying the read voltage vector across the drains and sensing the current on the sources (Extended Data Fig. 6a). Due to the non-ohmic I-V behavior of the device, only binary input vectors are viable for the VMM operations, which meets the requirement of memristive RBM and DBN. The VMM operation in Extended Data Fig. 6a can be written as

$$I_{sj} = \sum_i^m V_R v_i G_{ij}, \quad (5)$$

where  $G_{ij}$  is the conductance of the memristive device at the  $i$ th column and  $j$ th row of the  $m$ -by- $n$  array,  $v_i$  is the element of the binary input vector,  $V_R = 2V$  is the read voltage, and  $I_{sj}$  is the element of the output vector.

Due to the unipolar conductivity of the device, the implementation of the backward VMM is not straightforward. It can be conducted in the array by using the input vector to indicate whether we switch the source to the ground or float it, biasing all the drains to the read voltage, and sensing all the drain currents, as shown in Extended Data Fig. 6b. The backward VMM operation can be written as

$$I_{Di} = \sum_j^n V_R h_j G_{ij}, \quad (6)$$

where  $h_j$  is the element of the binary input vector and  $I_{Dj}$  is the element of the output vector.

The program/depression of the device in an array is straightforward since only the devices with a high program voltage on the drains and their sources grounded will be programmed. The devices with the drain or source floating will be prevented from the program operations, as shown in Extended Data Fig. 6c.

The erase/potential of the device in an array needs special care since the erase pulse on the source will affect all devices in the row, no matter if the drains of the devices are grounded or floating. The devices that do not need to be erased in the row, however, can be deselected by applying a deselection voltage ( $V_E' = 3.5V$ ) on the drains, as shown in Extended Data Fig. 6d.

**Memristive RBM demonstration.** The testing system containing two 12-by-8 memristive device arrays is used to demonstrate the training and inference of the RBM in Figure 3a. The RBM has two weight matrices:  $w_1$  with the size of 12-by-8 and  $w_2$  with the size of 7-by-8, which are instantiated by the two memristive arrays, Chip 1 and Chip 2, respectively, as shown in Figure 3c. To represent the signed weights, we use a separated row and a separated column of the memristive devices with the conductance of  $G_{ref}$  to subtract from the always positive conductance of the memristive array. For instance, as shown in Figure 3d about the forward VMM and stochastic sampling, the weight of each element in the weight matrix can be expressed as  $w_{ij} = G_{ij} - G_{ref}$ .

The training procedure of the memristive RBM is shown in Extended Data Fig. 8. The testing system performs VMM and weight updates in the memristive array. The stochastic sampling and the calculation and accumulation of the contrastive divergence (CD) are performed in software. For instance, the probability of the hidden units being excited is determined by

$$P(\mathbf{h} = 1) = \sigma(\mathbf{I}_h / I_0) \quad (7)$$

where  $I_{hj} = \sum_i^m V_R v_i G_{ij} - \sum_i^m V_R v_i G_{ref}$  is the current differences of the output from the VMM operation on the memristive device array,  $\sigma(\cdot)$  is the logistic function, and  $I_0$  ( $I_0 = 0.2\mu A$  in the RBM training) is the step parameter of the logistic function, which can be realized by controlling the intensity of the noise current<sup>40</sup> in Figure 3d. Note that the software operations can be fully implemented in hardware when integrated into an application-specific integrated circuit (ASIC).

**Memristive DBN simulation.** The simulation of the learning and inference of the memristive DBN uses the model of the memristive device, which nicely captures the device I-V behaviors, potentiation, and depression conductance updating behavior, cycling degradation, and device-to-device variations. The CD threshold for the training is set to 64 and -64, corresponding to signed 6-bit digital counters in the CD accumulation array. The step parameter of the logistic function in Eq. 7 is set to 1 uA ( $I_0 = 1\mu A$ ).

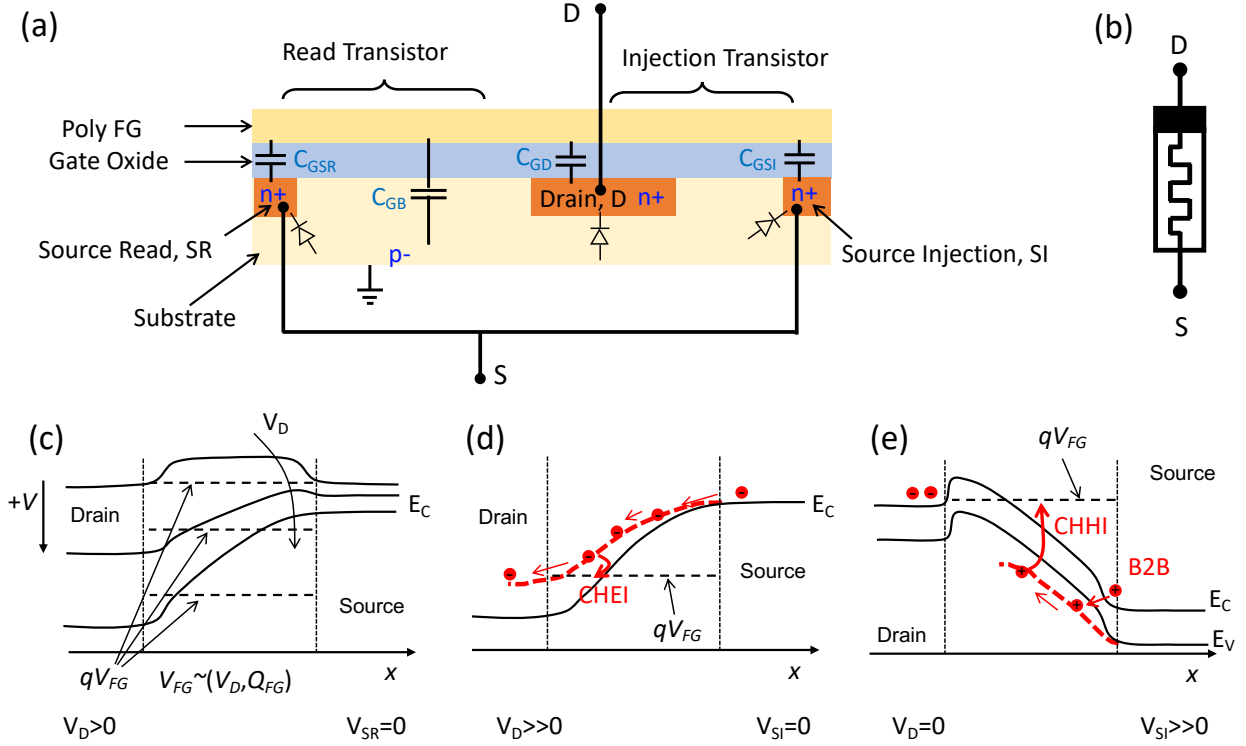
**DBN fine-tuning.** A fine-tuning procedure of the memristive DBN is performed using the wake-sleep algorithm<sup>42,43</sup> after the greedy-learning of the DBN (pretraining). To do the fine-tuning, the RBMs in the memristive DBN are duplicated, except for the last RBM, with the new weight matrices  $w_1=w_1'$  and  $w_2=w_2'$  (Figure 4a). The weight matrices  $w_1, w_2, w_3$ , and  $w_4$  constitute the recognition path and the weight matrices  $w_4, w_3, w_2'$ , and  $w_1'$  constitute the generation path or wake path. The input data of the image and the label are fed to the recognition path, and the top RBM layer performs Gibb sampling iteratively (iteration number is 20 in our simulation), and then the reconstructed visible neuron states are fed to the generation path to generate the reconstructed image (sleep path). The states of neurons in the wake path and sleep path are used to update the weight matrix in the sleep path and wake path, respectively. For the simulation results shown in Figure 4, the DBN is pre-trained for 30 epochs and fine-tuned for another 30 epochs

**Design of peripheral circuits.** The designed memristive RBM and DBN utilize mixed-signal learning: the memristive array conducts the VMMs and the stochastic sampling in the analog domain, and other parts of the system, including the CD accumulation and communication between adjacent RBM layers, work in the digital domain. The full peripheral circuit of the memristive array in the analog domain is designed and shown in Extended Data Figure 9. The peripheral circuit includes multiplexers, trans-impedance amplifiers, noise current generators, and comparators. No digital-to-analog converters (DACs) or analog-to-digital converters (ADCs) are needed in the peripheral circuit.

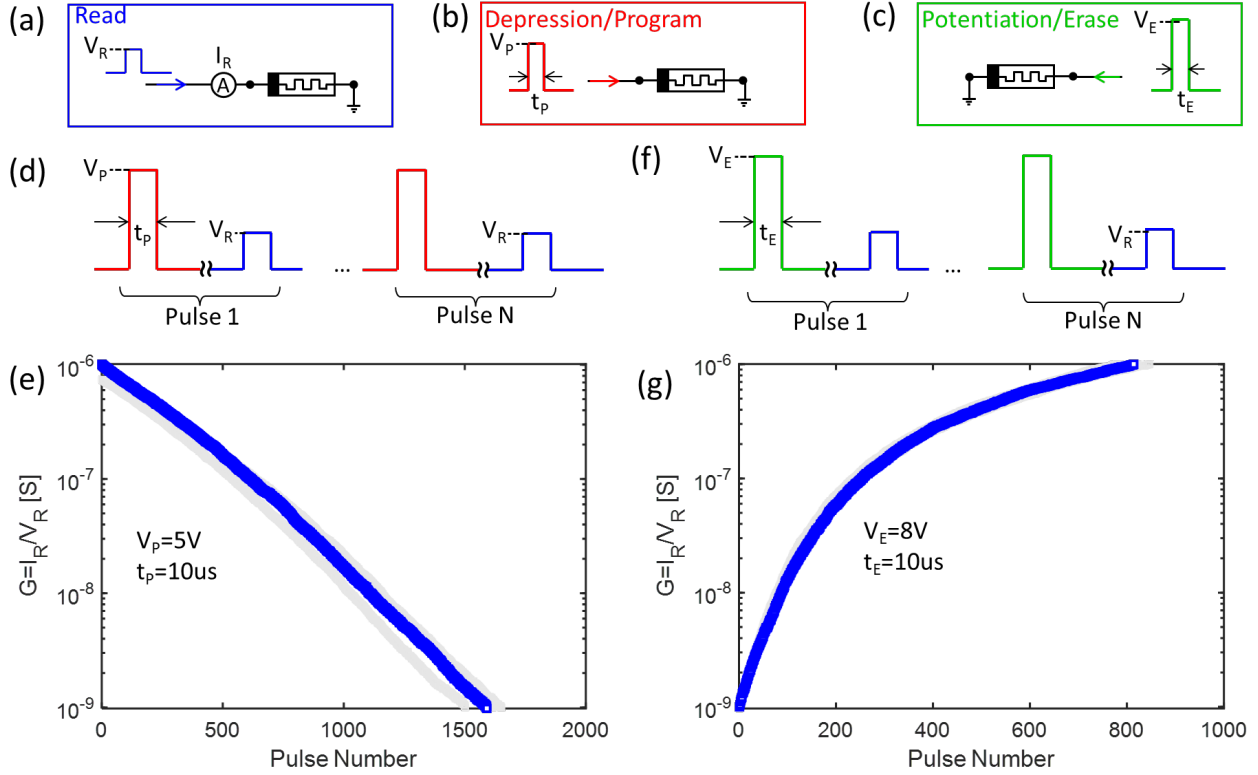
**Metric estimations.** A single device in an array has the footprint of  $2.7\mu m \times 1.17\mu m = 3.159\mu m^2$

(180 nm technology). The maximum energy consumption of the readout, program, and erase operations are estimated as  $2V \times 1\mu A \times 50ns = 0.1$  pJ,  $5V \times 20\mu A \times 200us = 20$  nJ, and  $8V \times 10nA \times 100us = 8$  pJ, respectively. Note that the actual energy consumption should be calculated according to the actual conductance states of the devices, which can be obtained from the neural network simulation. The weight update operations consume much more energy than the read operations since they need longer pulses, and the program/depression operations work in the transistor-on mode. However, since we use the CD array to accumulate the required weight updates, the number of weight update operations is substantially reduced, thus reducing the energy consumption. In the training of the memristive DBN shown in Figure 4, the VMM operations consume 18 nJ per training image, while the weight updates consume 33 nJ per training image for the first RBM layer (size: 784-by-500). This means that approximately only three weight update operations ( $33nJ / (20nJ + 8pJ) \times 2$ ) are performed for each image input. The energy consumption of the other layers is proportional to their array sizes.

A single VMM operation on the first RBM layer consumes 11 nJ and takes 50 ns, which performs  $784 \times 500 = 392,000$  multiply-accumulate (MAC) operations. This results in an energy efficiency of  $3.56 \times 10^4$  GOPs  $s^{-1}W^{-1}$ . The area of the memristive array is  $3.159 \mu m^2 \times (784+1) \times (500+1) \approx 1.24$  mm<sup>2</sup>, which gives the performance density of  $6.31 \times 10^3$  GOPs  $s^{-1}mm^{-2}$ . These metrics show roughly 350 times and 170 times improvement on energy efficiency and performance density, respectively, compared with Tesla V100 GPU in 12 nm technology (energy efficiency: 100 GOP  $s^{-1}W^{-1}$ , performance density: 37 GOP  $s^{-1}mm^{-2}$  for 16-bit floating-point number computing)<sup>26</sup>. Note that the energy consumption and footprint of the peripheral circuits are not included in the calculation. Also, note that scaling down the device will strongly improve the metrics.

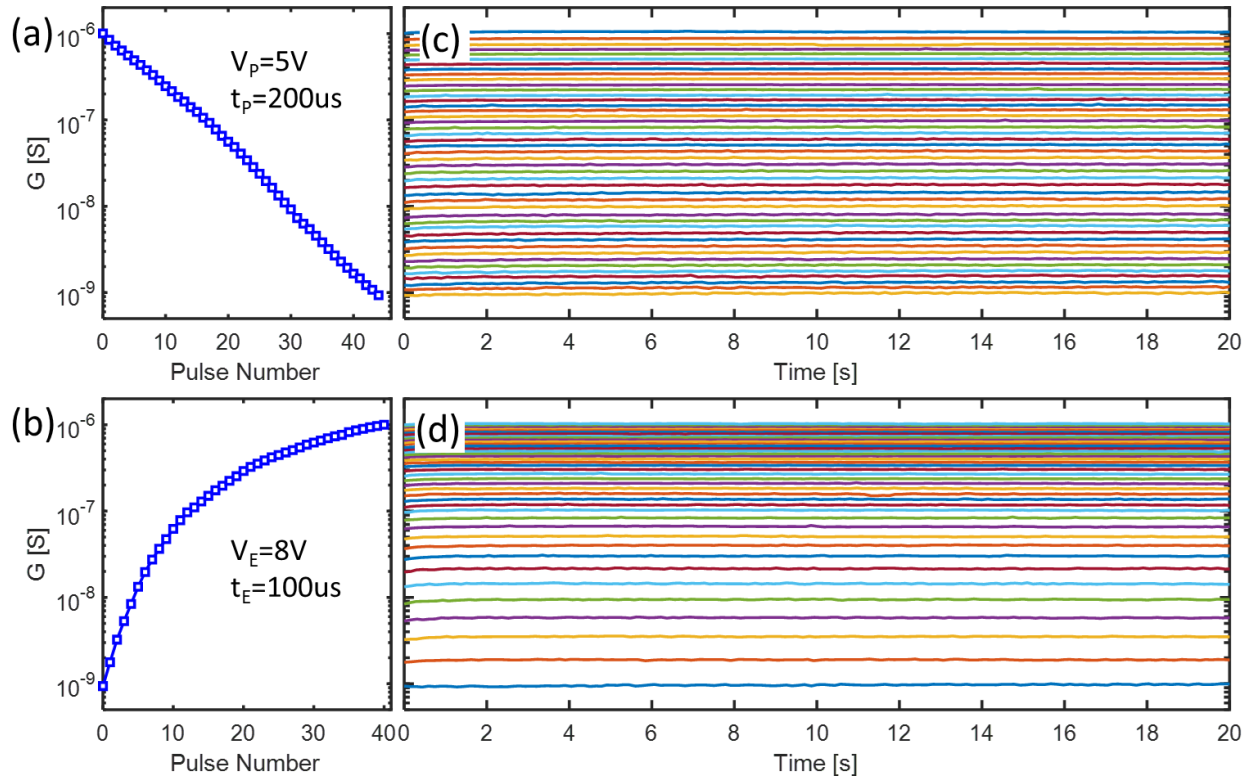


**Extended Data Fig. 1 | Device structure and band diagrams in different operational modes.** (a) Schematic illustration of the device structure from the sectional view. The injection transistor (shorter channel and higher threshold voltage) and the read transistor (longer channel and lower threshold voltage) are parallelly connected: they have a common drain and a common floating gate; their sources are externally shortened. The capacitance between the floating gate and the drain ( $C_{GD}$  is much larger than other capacitances), thus the floating gate voltage is mainly coupled to the drain. (b) The equivalent circuit symbol of the device. (c) Band diagrams of the read transistor in the reading mode. A low drain voltage will induce a low floating gate voltage and keep the transistor closed. As the drain voltage increases, the floating gate voltage increases, and the transistor gradually opens. The injection transistor shares similar behavior but has a lower current since the threshold voltage is higher. (d) The band diagram of the injection transistor at the depression (program) mode. When a higher voltage is applied to the drain and the source is grounded, the electrons in the channel are accelerated by the electrical field in the drain region, and the lucky ones are injected into the floating gate, i.e., channel hot electron injection (CHEI). (e) The band diagram of the injection transistor in the potentiation (erase) mode. When a higher voltage is applied to the source and the drain is grounded or floating, the source p-n junction is reversely biased. This induces band-to-band (B2B) hole generation in the source region. The high lateral electric field accelerates the generated holes, and the lucky ones are injected into the floating gate. The hot electron/hole effects are negligible in the readout transistor.

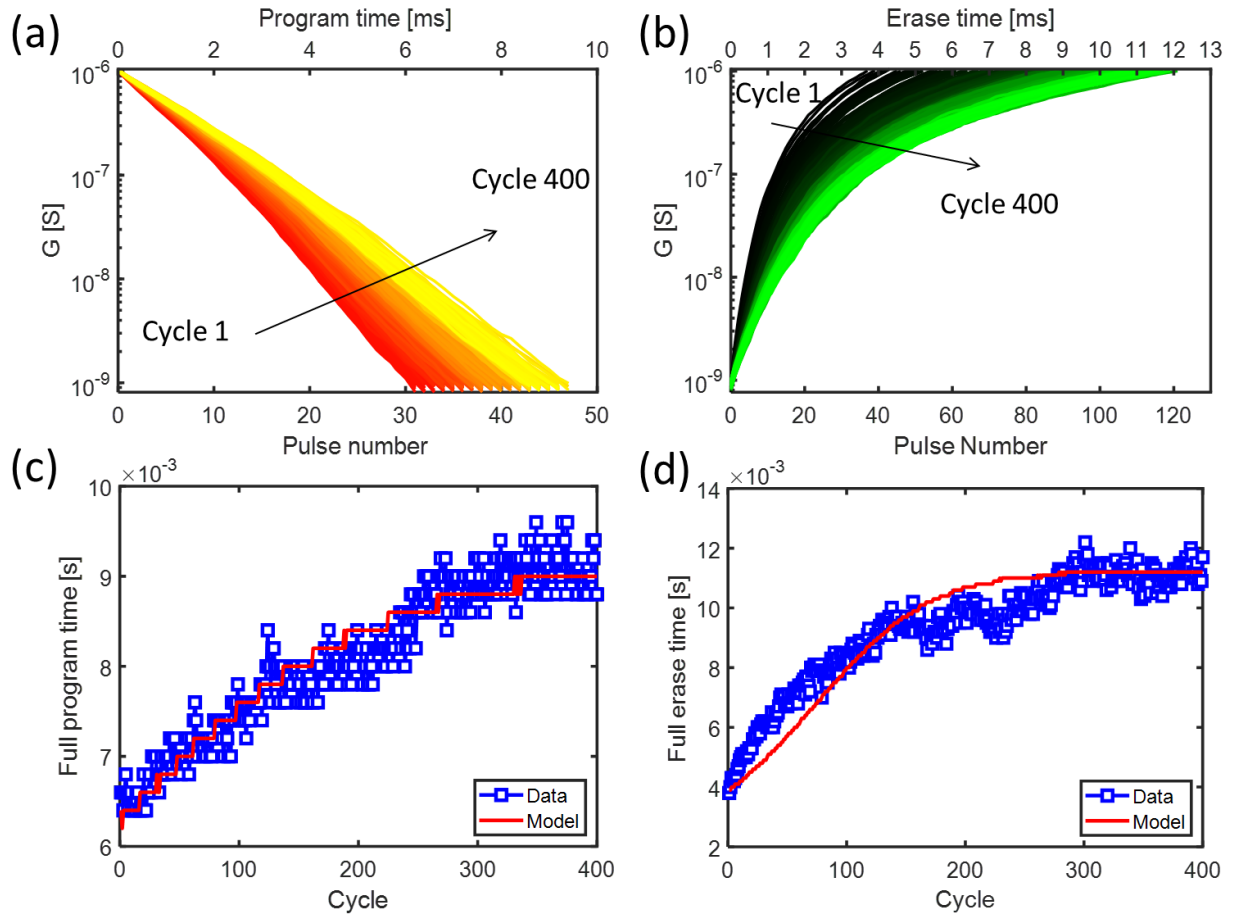


**Extended Data Fig. 2 | Depression and potentiation of the devices by continuous program or erase pulses.** (a) Read mode of the device by applying a voltage pulse ( $V_R=2V$  for pulse reading) on the D terminal and sensing the current ( $I_R$ ). (b) Depression (program) mode of the device operation by applying a voltage pulse ( $V_P=5V$ ) on the D terminal and grounding the S terminal. (c) Potentiation (erase) mode of the device operation by applying a voltage pulse ( $V_E=8V$ ) on the S terminal and grounding, or floating, the D terminal. The floating D terminal will be capacitively coupled to the grounded substrate. (d) Schematic of the pulse depression/program test by alternatively applying the program pulse and reading the device by the read pulse. (e) The device conductance ( $G=I_R/V_R$ ) as a function of the pulse number when depressing the device by programming pulses with the width of 10 us. (f) Schematic of the pulse potentiation/erase test by alternatively applying the erase pulse and reading the device by the read pulse. (g) The device conductance as a function of the pulse number when potentiating the device by erasing pulses with the width of 10 us.

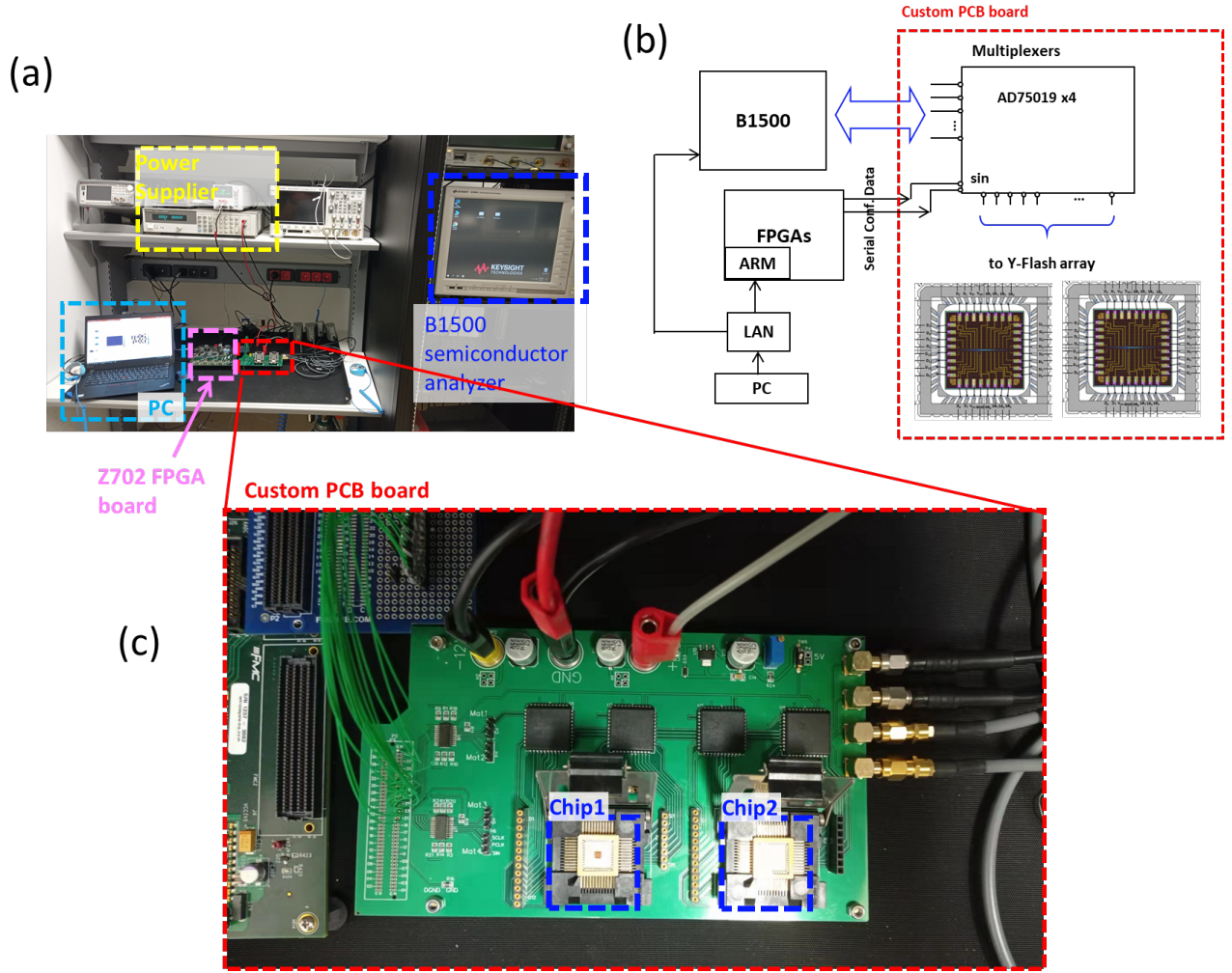




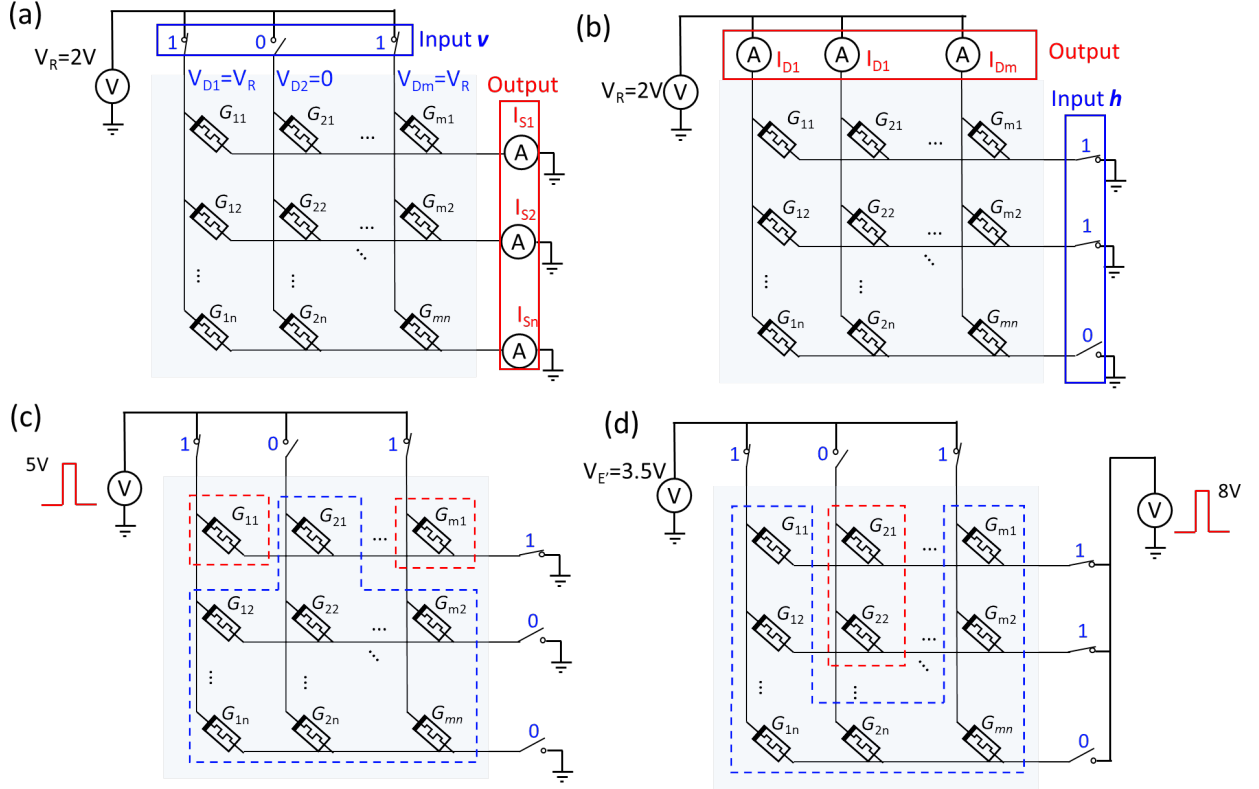
**Extended Data Fig. 3 | Depression, potentiation, and continuous readout operations of the devices.** (a) Depression (program) of the device by 200  $\mu s$  pulses. (b) Potentiation (erase) of the device by 100  $\mu s$  pulses. (c) The conductance of the device as a function of time after each program pulse by continuously reading the state of the device for 20 seconds. (d) The conductance of the device as a function of time after each erase pulse by continuously reading the state of the device for 20 seconds.



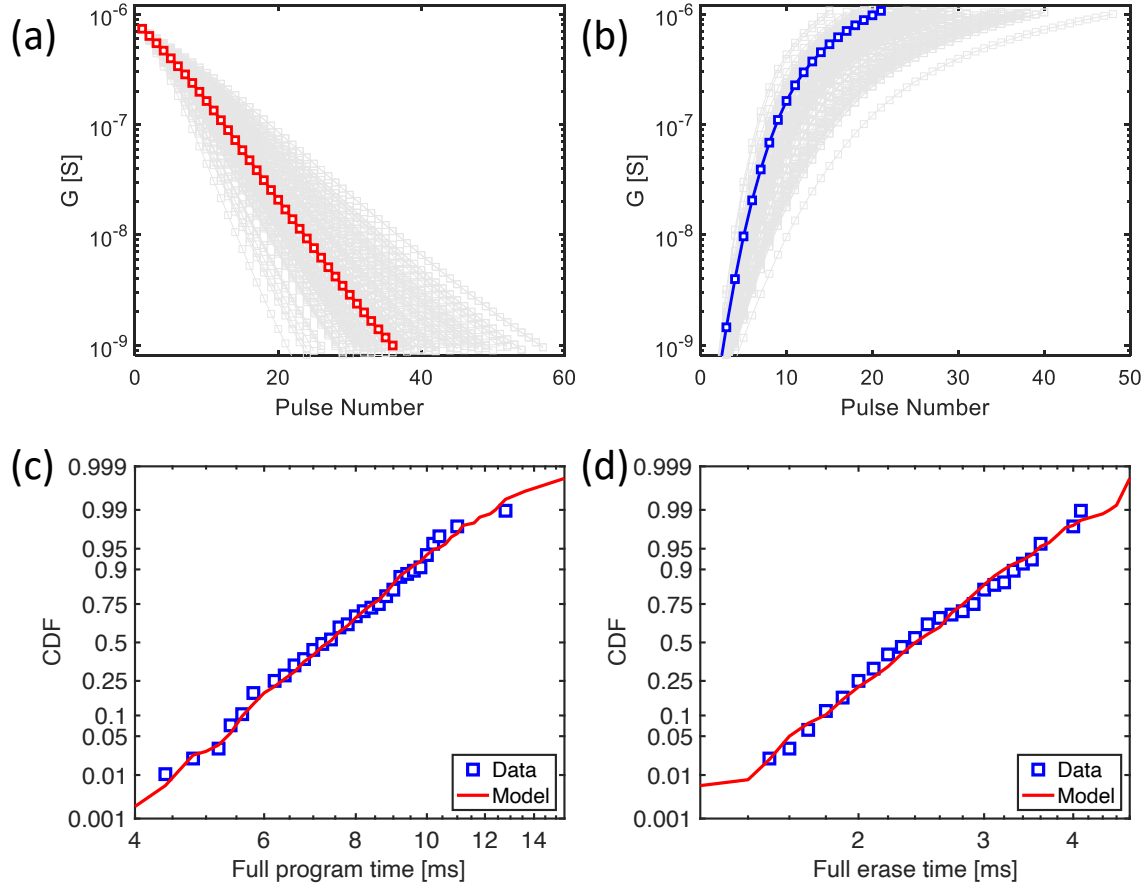
**Extended Data Fig. 4 | Cycling degradation and its modeling.** (a) Continuously depression/program of one device from the high conductance state (HCS) to the low conductance state (LCS) for 400 test cycles. (b) Continuously potentiation/erase of one device from the LCS to the HCS for 400 test cycles. (c) The program time (pulse number multiplied by the pulse width) needed for programming the device from HCS to LCS as a function of the cycling number. Both the experimental data and simulations results are presented in the figure. (d) The erase time needed for erasing the device from LCS to HCS as a function of cycling number.



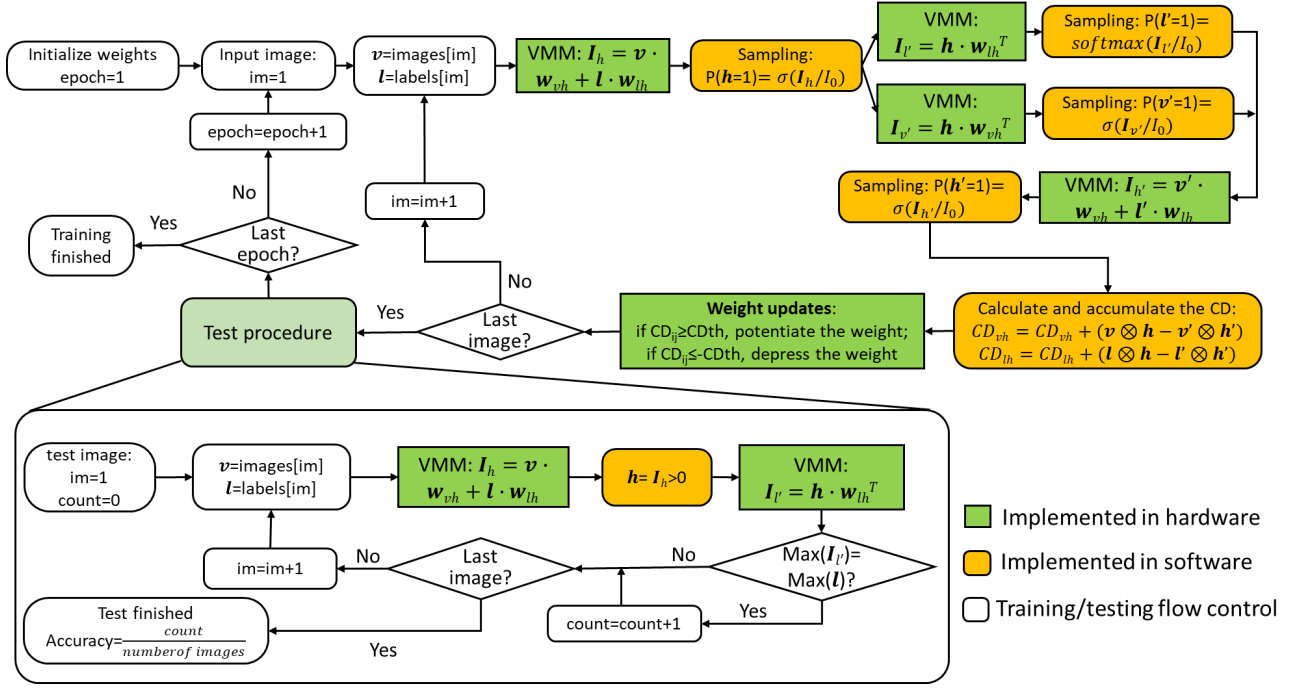
**Extended Data Fig. 5 | The setup of the test system for array operations and memristive RBM demonstration.** (a) Overview of the system consisting of a custom printed circuit board (PCB) board, a Z702 FPGA development board, a B1500 semiconductor analyzer, a controlling personal computer (PC), and power suppliers. (b) Schematic of the test system. (c) The details of the custom PCB board, which integrates two Y-Flash chips, each of which has a 12-by-8 array of two-terminal floating gate memristive devices.



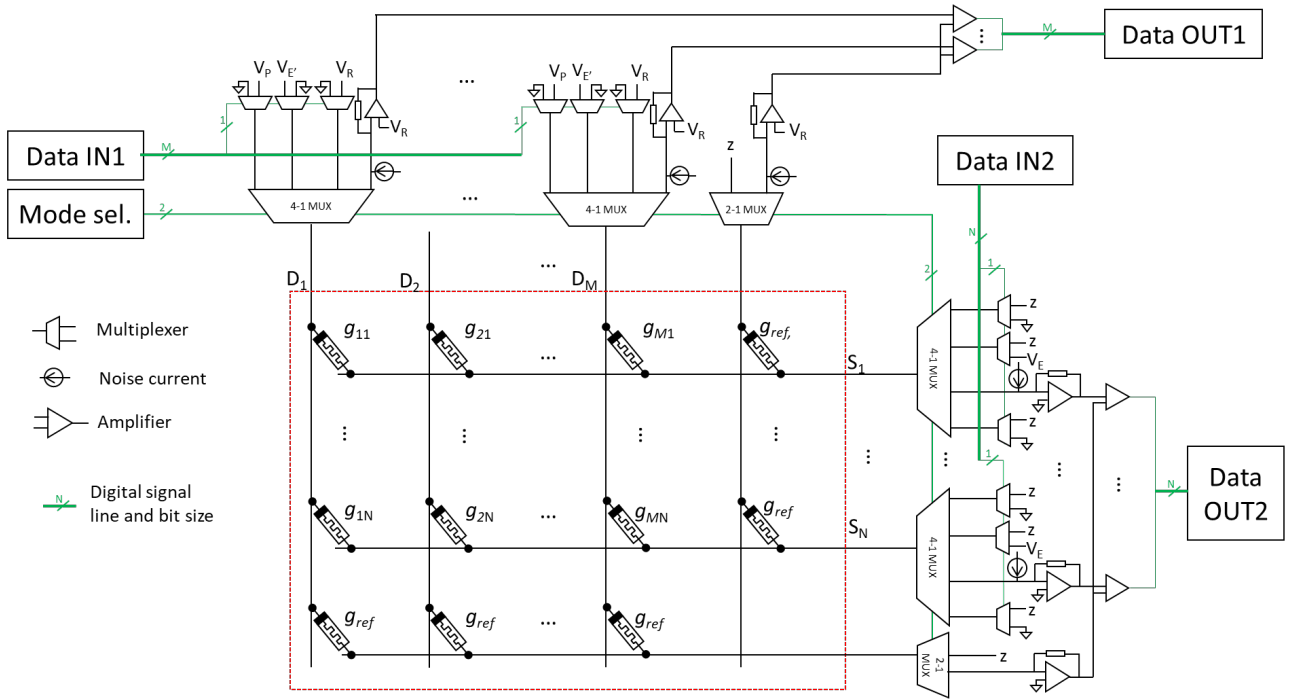
**Extended Data Fig. 6 | Read and write operations of the memristive devices in an array.** Schematics of performing (a) the forward VMM and (b) the backward VMM operations on an array of the two-terminal floating gate memristive devices. Schematics of performing (c) the depression/program operation and (d) the potentiation/erase operations on selected devices (marked by the red dashed line) in an array of the memristive devices.



**Extended Data Fig. 7 | Modelling of device-to-device variations.** (a) Simulated device-to-device variations of the depression/program behavior (red line: a typical depression curve; gray lines: all depression curve of other devices). (b) Simulated device-to-device variations of the potentiation/erase behavior. (c) Statistical result of total program times in different devices compared with simulation results. (d) Statistical result of total erase times in different devices compared with simulation results.



**Extended Data Fig. 8 | Flow chart of the online training of RBM including test algorithm after each training epoch.** The VMM and weight updates are performed in the memristive array using the testing system. The stochastic sampling, as well as the calculation and accumulation of the contrastive divergence (CD), are performed in software.



**Extended Data Fig. 9 | Full hardware design of the memristive part of an RBM layer.** The memristive part of an RBM layer conducts the forward and backward VMMs as well as the stochastic sampling in the analog domain. The peripheral circuit includes multiplexers, trans-impedance amplifiers, noise current generators, and comparators. No digital-to-analog converters (DACs) or analog-to-digital converters (ADCs) are needed in the peripheral circuit. Other parts of the memristive RBM and DBN are all digital circuits.